2002 HST Calibration Workshop
Space Telescope Science Institute, 2002
S. Arribas, A. Koekemoer, and B. Whitmore, eds.

Calibration Status of the Cosmic Origins Spectrograph Detectors

Steven V. Penton, Stéphane Béland, and Erik Wilkinson

Center for Astrophysics and Space Astronomy, University of Colorado, Boulder, CO 80309

Abstract. COS has two distinct ultraviolet channels covering the spectral range from 1150Å to 3200Å. The NUV channel covers the range from 1700Å to 3200Å and uses the Hubble Space Telescopes STIS spare MAMA. The FUV channel uses a micro channel plate detector with a cross-delay line readout system to cover the range from 1150Å to 1900Å. Due to the analog nature of the readout electronics of the FUV detector, this system is sensitive to temperature variations and has non-uniform pixel size across its sensitive area. We present a step-by-step description of the calibration process required to transform raw data from the COS into fully corrected and calibrated spectra ready for scientific analysis. Initial simulated raw COS data is used to demonstrate the calibration process.

1. Introduction

During the *HST* servicing mission currently scheduled for Spring 2005 (SM4), the Cosmic Origins Spectrograph (COS, Sembach 2002) is scheduled to be installed in the science bay currently occupied by COSTAR. COS contains two ultra-violet (uv) channels, which share two common 2.5″ diameter apertures (the primary science aperture, PSA, and the 1% transmission bright object aperture, BOA). The far uv (FUV, 1150–1900 Å) and the near uv (NUV, 1700–3200 Å) channels employ independent detectors but cannot be operated simultaneously. The one-bounce COS FUV channel uses holographic gratings to simultaneously disperse and correct the aberrated *HST* beam onto a two segment cross-delay line microchannel plate (MCP) similar to that flown on FUSE. The NUV channel uses a four-bounce optical path to disperse and correct the *HST* beam into three non-contiguous strips on a spare STIS MAMA detector. In this brief update on the calibration status of COS, we discuss the progress of the COS detector calibrations.

2. The FUV channel

The two FUV segments, 'A' and 'B', employ time-delay anodes in both the dispersion ('X') and cross-dispersion ('Y') directions. The anodes are used in conjunction with 85×10 mm MCP stacks (McPhate et al. 2000). The detectors do not have physical pixels, instead the time-delay detector represents the event location as an analog value. Each detector segment is represented $\sim 14,000 \times 400$ digital elements (DEs). The physical 'size' represented by each DE is variable across the detector. The background count rate is low, ~ 2 counts DE^{-1} month^{-1}. The FUV detector deadtimes are well characterized, and are $< 10\%$ at 10,000 counts s^{-1}. In this section, we will discuss the known distortions and the ground calibrations employed to correct them (Vallerga et al. 2001). Unless otherwise stated, the values discussed here are those for the 'A' segment of the 'FUV01' detector.

2.1. Thermal Distortions

The mapping function from reported photon location to DE value is temperature dependent. The thermal distortions, introduced prior to digitization, are well characterized as a combination of a shift and stretch of the position to pixel value mapping. Electronic stim pulses, representing events at fixed locations, are injected into the detector electronics and digitized as if actual photon events. The electronic stim pulses appear in the photon list at positions to the lower left and upper right of the MCP active area. To correct the photon list for thermal distortions, the lower left stim pulse position, and with it the rest of the photon list, is adjusted to a predetermined baseline position. The photon list is then stretched or compressed to force the upper right stim pulse position to fall at its baseline position. Results from the testing with the available ground flat field data (§2.3) suggest that this algorithm is more than sufficient for correcting the expected thermal distortions.

2.2. Geometric Distortion

As described in detail in Wilkinson, et al. 2001 and Béland et al. 2002, the mapping function from physical photon location on the FUV detector to analog DE value is not a straightforward linear mapping. Distortions in the FUV readout electronics and MCPs result in DEs of variable size. A typical row of the segment 'A' shows uncorrected DE sizes of $5.96 \pm 0.01\mu\text{m} \times 24.2 \pm 0.1\mu\text{m}$. To determine the geometric distortion correction (GDC), also referred to as the integral non-linearity (INL), an opaque mask with a regularly spaced grid of pinholes was imaged by the detectors. By comparing the known physical centers of the pinholes to their digital values, the GDC is determined for each segment. Since the DEs well sample the resolution element (RE, $\approx 6 \times 12$ DE), the physical size of the DEs can be forced to be a constant size of $6.0 \times 24.0\mu$m without affecting the scientific value (wavelength, resolution, etc.) of the detected events. The GDC is determined with thermally corrected data, and the correction is always applied after thermal correction. An opaque mask of slits was also imaged during ground testing, providing an independent method of determining the accuracy of the GDC. The GDC was applied to the measured position of the slits, and the known physical X position of the slits was then compared to the GDC corrected positions. These residuals show a Gaussian distribution with a residual error (1σ) of < 0.5 DE in the dispersion direction, corresponding to $\sim 1/12$ of a RE.

2.3. Flat Fields

During ground testing, 114 flat field images were obtained for each segment. These flat fields were thermally and geometrically corrected, then combined into deep flat fields (DFF) images. Each DFF contains $\sim 10^9$ photons, with a mean number of counts RE^{-1} of ~ 10000. These combined flat fields contain information on both the illumination of the detectors, the L-flat, and the DE-to-DE variations, the D-flat (or more traditionally, the P-flat). To separate the L and D-flats from the DFF, for each column (Y), the DFF was smoothed in the X direction, then a low-order polynomial function approximating the illumination pattern was fit along each column. The L-flat was constructed from the least-squares fits (assuming Poisson statistics), then the D-flat was derived by dividing the DFF by the L-flat. The signal-to-noise ratio, S/N, of the DFFs are ~ 100 RE^{-1}. A portion of the 'A' segment D-flat is shown in Figure 1. In this figure, the intensity scale has been modified to show the variations, the actual variations are Gaussian with a width of 5%. This implies that the flat-field variations must be removed to achieve COS FUV data with $S/N > 20$.

To test the quality of the flats, the original flat field images were randomly selected to create two independent DFFs for each segment. Each DFF was divided by the appropriate L-flat and D-flat to create two independent flatfielded test images. A 12 DE (Y) strip, shown in Figure 1, was extracted from each test image. The strips were collapsed per RE to form a spectrum following the same algorithm used for a spectral extraction. The two $S/N \sim 70$ RE^{-1} spectra were then divided to test the quality of the combined thermal, geometric, and

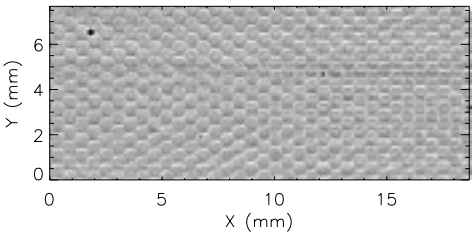

Figure 1. *D*-flat for a small section of the FUV segment 'A.' The intensity scale of the image has been modified to show variations. The actual variations are Gaussian with a width of $\approx 5\%$ ($S/N \approx 20$). The dashed lines indicate the 12 DE (Y) strip used to extract the simulated 'spectrum.'

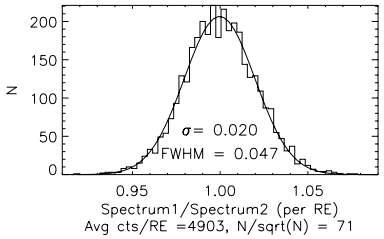

Figure 2. The DFF data set was divided into two independent data sets, each corrected for thermal, geometric, and flat field distortions. A strip of each test image was extracted as if a science spectrum. The 'spectra' were divided, with the above distribution indicating that COS FUV observations of $S/N = 50$ are achievable (or $S/N = 100$ if using FP-SPLIT = 4).

flat field extraction. The results of this test are shown in Figure 2. The resulting distribution is Gaussian with a width implying a final S/N of ≈ 50. This is indeed the expectation for two data sets limited only by Poisson statistics, $\sqrt{(1/70)^2 + (1/70)^2} \approx 1/50$. The data set was then dithered to approximate a FPSPLIT = 4 algorithm, with the expected result of a $S/N = \sqrt{4} \times 50 = 100$ extraction. COS contains an on-board flatfield lamp, which will be used on-orbit to achieve $S/N \geq 70$ RE^{-1} flatfields for the regions of the COS detector employed for obtaining scientific data.

2.4. Wavelength Accuracy

The limiting factor in wavelength accuracy is the ability to center targets in the aperture during target acquisition (TA). The COS TA algorithms have been tested with ray-trace simulations (Penton, 2001), and will be able to center the target in the aperture to within $0.1''$. This corresponds to a 3σ wavelength velocity error of less than 10 km s^{-1} for the FUV medium resolution gratings (64 km s^{-1} for the low resolution).

3. The NUV channel

The NUV detector is a STIS spare $1k \times 1k$ NUV MAMA, which has $25 \times 25 \mu$m pixels defined by physical structures in the anode. The thermal and geometric distortions of NUV detector are small, and will not require monitoring, calibration, or correction. Based upon ground measurements, and in-flight performance of the STIS MAMAs, the background count rate is expected to be ~ 34 counts s^{-1} cm^{-2} or 1.3 counts hour^{-1} pixel^{-1}. Following a flat-field procedure similar to that of the FUV channel, the measured NUV P-flat pixel distribution is Gaussian with a width of 0.044 ($S/N \sim 20$ pixel^{-1}). Extracting a spectral region gives a

Gaussian distribution with a $S/N \sim 50$ RE^{-1}, or $S/N \sim 100$ RE^{-1} for an FPSPLIT = 4 observation. Like the FUV channel, on-orbit NUV flat fields will be used for calibrating *HST*+COS NUV data. NUV wavelength accuracy is also limited by the TA centering accuracy. Simulations (Penton, 2001) indicate that the TA introduced 3σ wavelength error for medium resolution NUV observations should be < 19 km s^{-1} (200 km s^{-1} for low resolution).

4. Conclusions

Ground-based calibration data, combined with extensive modelling using our current understanding of the COS detectors and optical system, indicate that S/N of 100 observations should be possible with both COS channels. On-going calibrations are on schedule to provide the highest quality data with *HST*+COS. Some calibrations, such as measuring the sensitivity function, can only be performed on-orbit. More information on COS can be found at http://cos.colorado.edu and http://www.stsci.edu/instruments/cos. This work was supported by the *HST* COS project (NAS5-98043).

References

Béland, S., Penton, S. V., & Wilkinson, E., 2002, Proc. SPIE, in press, 2002

Sembach, K. R., et al. 2002, in *COS Instrument Mini-Handbook, version 1.0*, (Baltimore: STScI), available at http://www.stsci.edu/instruments/cos/cos_docs.html.

McPhate, J. B., Siegmund, O. H., Gaines, G., Vallerga, J. H., & Hull, J., 2000, *The COS FUV Detector*, Proc. SPIE 4139, 25

Morse, J. A., et al. 1998, *Performance overview and science goals of COS for HST*, Proc. SPIE 3356, 361, (also see COS-01-0001, available at http://cos-arl.colorado.edu/OP01/)

Penton, S. V. 2000, *TAACOS: Phase I FUV Report*, COS Internal Document, COS-011-0016, available at http://cos-arl.colorado.edu/TAACOS/

Penton, S. V. 2001, *TAACOS: Phase I NUV Report*, COS Internal Document, COS-011-0024, available at http://cos-arl.colorado.edu/TAACOS/

Vallerga, J. V., McPhate, J. B., Martin, A. P., Gaines, G. A., Siegmund, O. H., Wilkinson, E., Penton, S. V., & Béland, Stéphane, 2001, Proc. SPIE 4498, 141

Wilkinson, E. 2002, *COS Calibration Requirements and Procedures*, COS Internal Document, COS-01-0003, available at http://cos-arl.colorado.edu/AV03/

Wilkinson, E., Penton, S. V., Béland, S., Vallerga, J. V., McPhate, J., & Sahnow, D. J. 2001, Proc. SPIE, 4498, 267